An anisotropic micro-ellipsoid constitutive model based on a microstructural description of fibrous soft tissues

Laure Astruc, Annie Morch, Jean-François Witz, Vít Nováček, Frédéric Turquier, Thierry Hoc, Mathias Brieu

An anisotropic micro-ellipsoid constitutive model based on a microstructural description of fibrous soft tissues

Laure Astruc[a,*], Annie Morch[a], Jean-François Witz[a], Vít Nováček[b], Frédéric Turquier[b], Thierry Hoc[c], Mathias Brieu[a]

[a] *Univ. Lille, CNRS, Centrale Lille, FRE 2016 - LaMcube - Laboratoire de mécanique multiphysique multiéchelle, F-59000, Lille, France*
[b] *Medtronic, Sofradim Production, 116 avenue du Formans, 01600 Trévoux, France*
[c] *Université de Lyon, École Centrale de Lyon, 36 av Guy de Collongue, 69134 Écully Cedex, France*

Abstract

The aim of this paper is to propose a multi-scale anisotropic constitutive model based on a microscopic description of a soft fibrous tissue. The proposed model is based on directional (or micro-sphere) strain energy density, linking the contribution of fibers to macroscopic elasticity. The link between the microscopic fiber and the macroscopic response is obtained by homogenization involving numerical integration on the surface of the homogenized volume. Directly from the texture analysis of microscopic observations, anisotropy is accounted for an ellipsoid, used as the basis for integration. In each spatial direction of the summation, the initial length of the fibers is penalized according to the geodesic of the anisotropic ellipsoid. Unlike conventional models, anisotropy is taken into account for strains, which allows the mechanical properties of the fibers to be maintained throughout the elementary volume. A new specific integration scheme on an ellipsoidal surface was then developed to facilitate numerical implementation. The strains penalization also ensures that the solution obtained when increasing the amplitude of anisotropy is not degraded. This model, with the new integration method, has been tested for its relevance on numerical tissues. The objectivity and invariance of rotation were then proven. Finally experimental data obtained on human abdominal wall connective tissues were used to verify the accuracy of the results and the predictive capabilities of the model.

Keywords: constitutive behavior, anisotropic material, microstructure, biological material, soft tissue, hyperelasticity, directional model, micro-sphere model

1. Introduction

Controlling the behaviour of biological tissues has become a major challenge. Thanks to numerical simulation, behaviour under physiological or pathological loading is understood and predicted, offering benefits in many areas: improvement of surgical techniques (Guérin and Turquier, 2013) or medical devices

*Corresponding author
Email address: laure.astruc@centralelille.fr (Laure Astruc)

(Lister et al., 2011) or risk prediction for patients (Mayeur et al., 2017), allowing specific accessible treatment. For example, for a patient, the predictive numerical model will be used to choose one surgical method over another, with a customized surgical device, depending on the potential complications.

To achieve patient-specific simulation and improve medical treatments, it is necessary to characterize and model the mechanical behaviour of the tissues involved in the treatment. Classically, the macroscopic mechanical behaviour of biological soft tissues is characterized by several hyperelastic models (Mooney, 1940; Rivlin, 1948; Ogden, 1978; Yeoh, 1993). However, these models derive from purely phenomenological functions of strain energy, considered isotropic (Chagnon et al., 2015; Wex et al., 2015): they are used as a first approach and because of their ease of implementation. Hostettler et al. (2010), Abraham et al. (2011) and Silva et al. (2017) used a Mooney-Rivlin or a Yeoh model to characterize the mechanical properties of the liver, the pelvic floor and the meniscal attachment while a Ogden model was used to characterize the skin (Lapeer et al., 2010), the brain Kaster et al. (2011), the liver (Lister et al., 2011) and the bladder and rectum (Boubaker et al., 2015). Human connective tissues are heterogeneous, composed of an intertwining of collagen and elastin fibers. This entanglement leads to highly anisotropic hyper-elastic non-linear behaviour (Korenkov et al., 2001; Astruc et al., 2018). In recent years, this constitutive phenomenological modeling has incorporated a microstructure-based approach to include some parameters with a more physical meaning (Holzapfel et al., 2015; Polzer et al., 2015; Brieu et al., 2016). The most commonly used model is the generalized structure tensor (GST) model, which includes a scalar structure parameter representing the fiber distribution (Gasser et al., 2006; Li et al., 2018). Such models therefore assume a predetermination of anisotropy with *a priori* preferential directions and introduce many material and geometric parameters leading to difficult parameters identification and numerical implementation. In case of anisotropic biological tissues such as the abdominal connective tissues, anisotropy predetermination is not possible because of its patient-dependency and its variation according to location (Gräßel et al., 2005; Astruc et al., 2018). A model where the directions of anisotropy are directly identifiable variables is lacking. The second commonly used class of model is the directional approach (also called micro-sphere), based on a spatial arrangement of weighted fiber bundles homogenized by integration on the surface of the unit sphere, either isotropic (Miehe et al., 2004) or anisotropic (Alastrué et al., 2009a). In this approach structural information is included assuming a fiber orientation distribution function (ODF).

Bergonnier et al. (2005) then Witz et al. (2008) found a clear link between image texture and linear elastic behaviour. For textured material as crimped glass wool, elastic properties were identified directly from quantitative images analysis of the heterogeneous texture of the sample. In this study, we propose to extend this approach to non-linear 3D hyper-elastic behavior. Images of tissues at the fiber scale were obtained using multiphotonic microscopy. Then texture analysis of the whole image gives access to the main orientation and the disorientation rate, i.e. the anisotropy rate. By applying the structure tensor method developed by Rao and Schunck (1991), the 3D texture gives an image of the anisotropy of the tissue in

the form of an ellipsoid, oriented along the main direction and whose minor axes correspond to the rate of disorientation of the fibers in space.

Biological tissues, composed of polymeric fibers, can be assimilated to hyperelastic macromolecular network (Brieu et al., 2016). It is then possible to use formulations developed for long-chain macromolecular network (Wang and Guth, 1952; Arruda and Boyce, 1993; Kuhl et al., 2005). Each type of fiber is described by physically-based parameters related to its macromolecular properties, *i.e.* its material properties. Based on the formalism of (Brieu et al., 2016) for the isotropic directional model, the microstructure can be taken into account by integrating on the surface of the ellipsoid representing the anisotropy. With such an approach, material and microstructural parameters are independent and uncorrelated. Material (intrinsic) parameters can be determined while microstructural (extrinsic) parameters can be identified from the texture analysis according to the location of the tissue and the patient. Anisotropy is accounted by changing the fibers initial length according to the ellipsoid geodesic, which means that anisotropy only impacts the structure of the tissue and not its intrinsic properties. The studied tissue is considered as composed of similar unit elements, *i.e.* the fiber, with the same intrinsic properties, only the spatial arrangement of the unit elements confers the extrinsic properties to the entire tissue. Moreover, unlike the micro-sphere model, working in deformation rather than stress avoids an increase in the number of integration points in the event of very significant anisotropy (Alastrué et al., 2009b; Verron, 2015), allowing implementation in finite element code with reasonable calculation times.

The purpose of this paper is to propose a multi-scale anisotropic constitutive model based on a directional strain energy density, using a microscopic description of the tissue to predict its macroscopic behaviour. One of the main interests lies in the limited number of parameters. The intrinsic parameters, linked to the material, are set common to all individuals and the extrinsic parameters, linked to the microstructure, are the only variable information. The first part describes the modeling framework and in particular the strain energy density integrated on the surface of a volume directly coinciding with the anisotropy of the tissue. A new method of integrating over a revolution ellipsoid surface is then proposed. The second part deals with the validation of the model, with several cases of anisotropy. The third part focuses on its application to experimental tests on human abdominal rectus sheath and the demonstration of the model's ability to identify the microstructure by setting constant material parameters.

2. Theoretical study

2.1. Constitutive equations

Biological fibrous soft tissues have an anisotropic hyper-elastic response (Martins et al., 2012; Astruc et al., 2018). To model the hyper-elastic behavior under large strains, a strain energy density $\mathcal{W}$ is introduced to formulate constitutive equations. The deformation gradient tensor $\boldsymbol{F}$ allows to describe the transformation

from an initial configuration to a deformed one. Stresses may be expressed with the second Piola-Kirchhoff stress tensor, $\boldsymbol{S}$, as:

$$\boldsymbol{S} = \frac{\partial \mathcal{W}}{\partial \boldsymbol{E}} - p\boldsymbol{C}^{-1} \tag{1}$$

with $\boldsymbol{C} = \left(\boldsymbol{F}^T.\boldsymbol{F}\right)$, the right Cauchy-Green strain tensor and $\boldsymbol{E} = \frac{1}{2}\left(\boldsymbol{C} - \boldsymbol{I}\right)$, the Green-Lagrange strain tensor. p is a Lagrange multiplier, treated as a hydrostatic pressure resulting from the incompressibility assumption of the tissue. Incompressibility also implies:

$$det(\boldsymbol{C}) = 1 \tag{2}$$

A biological tissue is a polymer constituted of fibers (Gräßel et al., 2005), considered as a spatial network of fibers, spread in every directions of space. Treloar and Riding (1979) proposed a full network model assuming that each spatial direction $\underline{u}$ contributes to the global elasticity of the material. The strain-energy function, $\mathcal{W}$, is obtained by a summation over all directions, $\underline{u}$, on the spatial material layout $\mathcal{S}$ of the elementary strain energy densities, w, related to the contribution of fiber aligned with $\underline{u}$:

$$\mathcal{W}(\boldsymbol{C}) = \frac{1}{\mathcal{S}} \iint_{\mathcal{S}} w(\lambda(\boldsymbol{C}, \underline{u}))d\mathcal{S} \tag{3}$$

where λ is the stretch measure seen by the direction $\underline{u}$ (Arruda and Boyce, 1993; Diani et al., 2004):

$$\lambda = \sqrt{\underline{u}.\boldsymbol{C}.\underline{u}} \tag{4}$$

In order to obtain a microstructurally-based modeling of the behavior, the model is based on a physical description of the fibers. A form of w was introduced by Kuhn and Grün (1942), with a single-chain probability density function:

$$w_{sc}(\lambda, N) = \kappa_B T N \left(\beta(\lambda)\frac{\lambda}{\sqrt{N}} + ln\left(\frac{\beta(\lambda)}{sinh(\beta(\lambda))}\right)\right) \text{ with } \beta(\lambda) = \mathcal{L}^{-1}\left(\frac{\lambda}{\sqrt{N}}\right) \tag{5}$$

which, after derivation, brings to:

$$\frac{\partial w_{sc}(\lambda, N)}{\partial \lambda} = \kappa_B T \sqrt{N} \mathcal{L}^{-1}\left(\frac{\lambda}{\sqrt{N}}\right) \tag{6}$$

where κ_B is Boltzmann's constant and T the absolute temperature. N is the average length of the macromolecules, with $\sqrt{N}$ the limit of extension of the chains and the function $\mathcal{L}^{-1}$ is the inverse of the Langevin's function: $\mathcal{L}(x) = coth(x) - 1/x$, generally approximated by Padé approximant (Cohen, 1991; Jedynak, 2015) or a Taylor serie, chosen as long as λ is not to close to the limit of extension (Gillibert et al., 2010). The total chain energy density derivative per unit volume is then:

$$\frac{\partial w(\lambda, C, N)}{\partial \lambda} = C \sqrt{N} \mathcal{L}^{-1}\left(\frac{\lambda}{\sqrt{N}}\right) \tag{7}$$

where $C = n\kappa_B T$ with n the chain density per unit reference volume (Arruda and Boyce, 1993; Diani et al., 2006). C is homogeneous to a stress and is therefore treated as the rigidity of the chains.

The elastic energy density partial derivative from Eq. (3) with (1) comes as:

$$\frac{\partial \mathcal{W}}{\partial \boldsymbol{C}} = \frac{2}{\mathcal{S}} \iint_{\mathcal{S}} \frac{\partial w(\lambda)}{\partial \lambda} \frac{\partial \lambda}{\partial \boldsymbol{C}} d\mathcal{S} \tag{8}$$

By substitution of Eq. (7) in (8), the expression of the second Piola-Kirchhoff stress tensor becomes:

$$\boldsymbol{S} = \boldsymbol{S'} - p\boldsymbol{C}^{-1} \tag{9}$$

with :

$$\boldsymbol{S'} = \frac{1}{\mathcal{S}} \iint_{\mathcal{S}} \frac{C\sqrt{N}}{\lambda} \mathcal{L}^{-1}\left(\frac{\lambda}{\sqrt{N}}\right) (\underline{u} \otimes \underline{u}) \, d\mathcal{S} \tag{10}$$

However a problem occurs with this formulation in its initial state, for $\boldsymbol{F} = \boldsymbol{I}$. The directional invariant does not allow a state free of stress, the addition of a prestress is therefore required to ensure an unloaded state (Diani et al., 2004; Kuhl et al., 2005). In literature, few studies (Criscione et al., 2002; Ciarletta et al., 2011) have examined the development of structural invariants ensuring a stress free initial state while others (Chagnon et al., 2015) have used higher-order functions involving structural invariants. Similarly, the structural invariant used in this study, directional elongation, can be modified to ensure a stress free state without pretension. In order to maintain the use of the Langevin inverse function as extensibility function, the new structural invariant becomes:

$$\nu(\boldsymbol{E}, \underline{u}) = (\underline{u}.\boldsymbol{E}.\underline{u})^2 + 1 \tag{11}$$

as a function of $\boldsymbol{E}$, derived from the directional stretch and adapted to ensure an unloaded state in the initial configuration, for the stress tensor part $\boldsymbol{S'}$ in Eq. (9) expressed by:

$$\boldsymbol{S'} = \frac{2}{\mathcal{S}} \iint_{\mathcal{S}} C\sqrt{N}\sqrt{\nu - 1} \, \mathcal{L}^{-1}\left(\frac{\nu}{\sqrt{N}}\right) (\underline{u} \otimes \underline{u}) \, d\mathcal{S} \tag{12}$$

This form of the stress tensor depends on only two material (intrinsic) parameters, C and N and equals zero at zero deformation by definition. Moreover, considering a higher order deformation function allows us to achieve the same objectives as in worm-like chain models (Kuhl et al., 2005): the unitary element is not loaded in the same way as the global tissue. During uniaxial traction, not all fibers are directly recruited: the fiber does not deform as quickly as the overall tissue and is recruited in a more non-linear way. The deformation measurement thus modified therefore makes it possible to take this phenomenon into account, without the addition of parameters.

Thereafter, we will work with the first Piola-Kirchhoff stress tensor τ, also called the nominal stress tensor, expressing the experimentally measurable stress, as:

$$\boldsymbol{\tau} = \boldsymbol{F}\boldsymbol{S} = \frac{2\boldsymbol{F}}{\mathcal{S}} \iint_{\mathcal{S}} C\sqrt{N}\sqrt{\nu - 1} \, \mathcal{L}^{-1}\left(\frac{\nu}{\sqrt{N}}\right) (\underline{u} \otimes \underline{u}) \, d\mathcal{S} - p\boldsymbol{F}^{-\boldsymbol{T}} \tag{13}$$

2.2. Analytical solution

In order to conduct analytical solutions, we consider an uni-axial tensile test performed according a given loading direction, with an imposed stretch and a sought stress, on an anisotropic soft tissue sample with arbitrary material properties, C and N, with an unidentified material reference.

The Cauchy stress tensor $\boldsymbol{\sigma}$, also named the true stress tensor, defined in the principal stresses reference $(\underline{e_{\sigma_I}}, \underline{e_{\sigma_{II}}}, \underline{e_{\sigma_{III}}})$ (*i.e.* the load reference) is, for an uni-axial load in the $\underline{e_{\sigma_I}}$ direction:

$$\boldsymbol{\sigma} = \begin{pmatrix} \sigma_I & 0 & 0 \\ 0 & \sigma_{II} = 0 & 0 \\ 0 & 0 & \sigma_{III} = 0 \end{pmatrix}_{(\underline{e_{\sigma_I}}, \underline{e_{\sigma_{II}}}, \underline{e_{\sigma_{III}}})} \tag{14}$$

Because of anisotropy, the principal stresses reference and the principal strains reference are not necessarily coincident. They coincide only in case of isotropy or when loading direction corresponds to material direction. Then the deformation gradient tensor $\boldsymbol{F}$ can be expressed in the principal stresses reference as:

$$\boldsymbol{F} = \begin{pmatrix} F_{11} & F_{12} & F_{13} \\ F_{21} & F_{22} & F_{23} \\ F_{31} & F_{32} & F_{33} \end{pmatrix}_{(\underline{e_{\sigma_I}}, \underline{e_{\sigma_{II}}}, \underline{e_{\sigma_{III}}})} \tag{15}$$

where F_{11} is known as the elongation sustained by the material in the loading direction. The others 8 F_{ij} components of the tensor are unknown. Eq. (14) and (15) provide the first Piola-Kirchhoff stress tensor $\boldsymbol{\tau}$ as:

$$\boldsymbol{\tau} = J\boldsymbol{\sigma}\boldsymbol{F}^{-T} = \begin{pmatrix} \sigma_I(F_{22}F_{33} - F_{23}F_{32}) = \tau_{11} & \sigma_I(F_{23}F_{31} - F_{33}F_{21}) & \sigma_I(F_{21}F_{31} - F_{22}F_{31}) \\ 0 & 0 & 0 \\ 0 & 0 & 0 \end{pmatrix}_{(\underline{e_{\sigma_I}}, \underline{e_{\sigma_{II}}}, \underline{e_{\sigma_{III}}})} \tag{16}$$

where τ_{11} is the experimental stress as $\tau_{11} = \dfrac{F}{S_0}$, with F the recorded force in N and S_0 the measured initial cross section in mm^2. $\boldsymbol{\tau}$ can then be re-expressed only according to F_{ij} and τ_{11} in terms of:

$$\boldsymbol{\tau} = \begin{pmatrix} \tau_{11} & \tau_{11}\dfrac{(F_{23}F_{31} - F_{33}F_{21})}{(F_{22}F_{33} - F_{23}F_{32})} & \tau_{11}\dfrac{(F_{21}F_{31} - F_{22}F_{31})}{(F_{22}F_{33} - F_{23}F_{32})} \\ 0 & 0 & 0 \\ 0 & 0 & 0 \end{pmatrix}_{(\underline{e_{\sigma_I}}, \underline{e_{\sigma_{II}}}, \underline{e_{\sigma_{III}}})} \tag{17}$$

The management of the incompressibility is achieved by the introduction of p (Eq. (1)). Finally, the system presents 10 unknowns: τ_{11}, p and F_{ij} (except F_{11}). With Eq. (13), we obtain 9 equations, from the tensor components, binding F_{ij}, τ_{11} and p. The incompressibility equation Eq. (2), linking the $\boldsymbol{F}$ components, provides the additional equation, rendering the problem solvable.

For any solicitation in a given direction, we can assess the mechanical stress exerted on the material and the related deformation gradient tensor.

2.3. Material anisotropy

Directional models (or micro-sphere models) were previously developed on isotropic (Miehe et al., 2004; Brieu et al., 2016) or Mullins softening induced anisotropic (Göktepe and Miehe, 2005; Merckel et al., 2013) materials. Such materials are organized in a three-dimensional network of long chains. Each chain is described with an elementary strain energy density with the same mechanical properties, C and N that contributes equally to the material, constituting an isotropic three-dimensional lattice. The global strain energy density is obtained by integration over the unit sphere according to Eq. (3). For computational time aspects, discrete distributions with a finite number of directions are introduced (Wang and Guth, 1952; Arruda and Boyce, 1993). Bažant and Oh (1986) directional integration networks are traditionally used, in particular the 2x21 $\underline{u_i}$ directions network, providing a good precision of the integral. In this study, the 2x66 network is chosen for its accuracy and efficiency (Gillibert et al., 2010). The discretized strain energy density is expressed as the summation of each elementary strain energy density w_i of direction $\underline{u_i}$, weighted by the integration weights ω_i:

$$\mathcal{W}(\boldsymbol{E}) = \sum_{i=1}^{M} \omega_i w(\nu(\boldsymbol{E}, \underline{u_i})) \tag{18}$$

In case of an anisotropy resulting from Mullins effect, the same set of directions is chosen according to the initial isotropy and the integration weights of the loading direction is penalized with an anisotropic damage law (Diani et al., 2006). The network remains spherical but the penalty allows to induce the anisotropy. In case of anisotropic materials, anisotropy ought to be taken into account from the outset. Micro-sphere models (Alastrué et al., 2010) depict the dispersion of fibers with the Bingham (Bingham, 1974; Spronck et al., 2016) or Von Mises ODF, assigning to each direction of the unit sphere an orientation concentration factor (Sáez et al., 2016).

The proposed model reflects the dispersion directly on the three-dimensional network. Texture analysis with the structure tensor method (Krause et al., 2010; Knutsson et al., 2011) establishes a distribution of the spatial orientations of the observed anisotropic sample (Fig. 1-A), from which an ellipsoid reflecting the anisotropy of the material is created (Fig. 1-B): the main direction of the ellipsoid coincides with the main directions of the fibers and the semi-minor axis coincides with the distribution width σ. The greater the anisotropy, the smaller the variance of the distribution, the thinner the integration ellipsoid becomes.

The ellipsoid is then used as an homogenization alternative to the unit sphere. Instead of considering an homogeneous network such as the unit sphere, the network is deformed according to the ellipsoid of revolution determined by image analysis. The vector materializing the direction $\underline{u_i}$ is no longer a unit vector, but its norm is correlated to the geodesic of the ellipsoid: a vector oriented in the direction of the major axis of the ellipsoid has a unitary norm while a vector oriented in the orthogonal plane, containing the minor axis, has a norm equal to R (Fig. 1-B). Physically, this is equivalent to locally changing the initial length of the fibers when projecting deformations on the directions (Eq. (11)), and not their stiffness as in

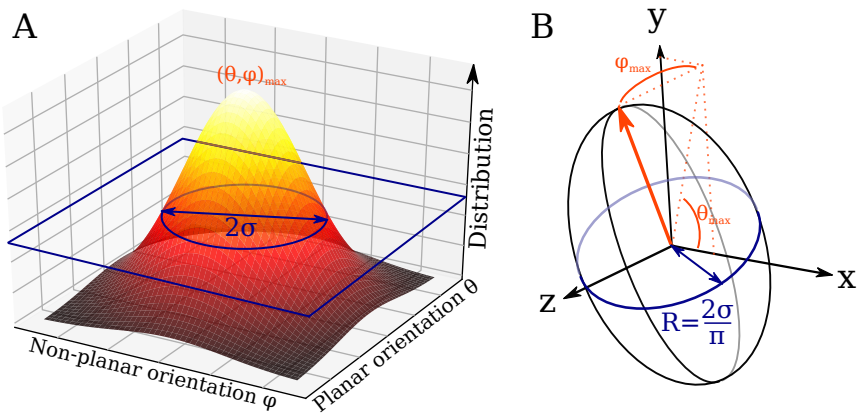

Figure 1: (A)-Gaussian type distribution of the spatial orientations of a transverse isotropic sample fibers and (B)-its related revolution ellipsoid: the major axis of the ellipsoid is oriented in the direction of the most represented orientation $(\theta, \varphi)_{max}$ and the minor axis length corresponds to the Gaussian variance σ.

conventional models with ODF. The ellipsoid maintains the mechanical properties of the fibers, the average length N and the density n, proportional to the stiffness C, and angularly varies the initial lengths of the fibers along the geodesic of the ellipsoid. The deformation applied to the network impacts only the direction and the norm of the network, in other terms the structure, but not the material properties of each direction. The intrinsic properties, *i. e.* the chains properties C and N, are not modified. Only the extrinsic properties are modified, namely the properties related to its structure, the initial length in each direction, which will vary according to the degree of anisotropy indicated. In this study, only transverse isotropy is considered. In case of a different anisotropic nature, an ordinary ellipsoid would be considered with two different minor axes, correlated to the particular distribution of the spatial orientations.

2.4. Numerical integration

Previous works (Bažant and Oh, 1986; Heo and Xu, 2001) used different schemes to evaluate integrals over the surface of a sphere providing accurate results. However, these methods cannot be used for ellipsoids. Pre-defined networks on the spheres cannot be deformed into ellipsoids. The distribution of integration points, homogeneous on the surface of a sphere (Fig. 2-A), is indeed no longer uniform once the sphere is deformed into an ellipsoid.

A customized integration scheme has therefore been developed to evaluate integrals over a revolution ellipsoid, allowing to select privileged directions. The directions are then chosen arbitrarily or according to the material microstructure. Fig. 2-B shows a specific distribution on a sphere, which can be easily applied to discontinuous materials with specific directions such as textiles (Morch et al., 2019). For anisotropic material, the parameterization of the surface, by angular discretization provides uniform distribution of the integration points on the revolution ellipsoid surface (Fig. 2-C).

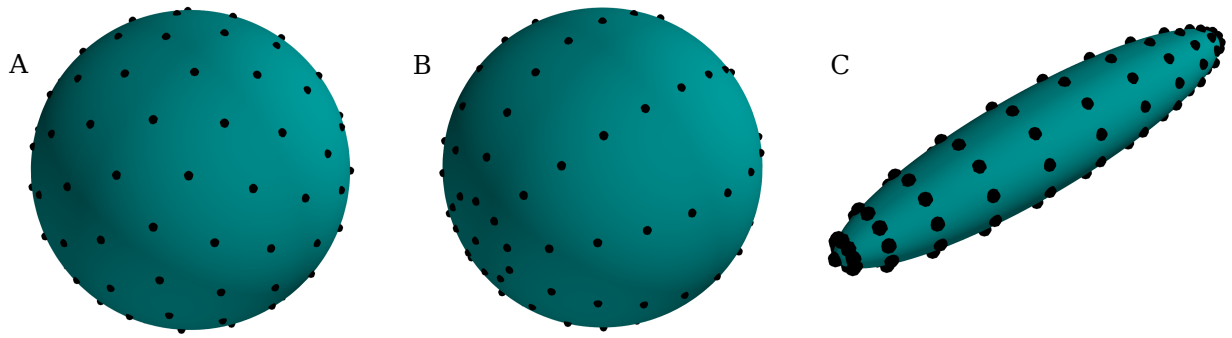

Figure 2: Comparison of the distribution of the integration directions over a sphere with the 122-directions set of Bazant-(A) and over a sphere-(B) and a revolution ellipsoid-(C) with the customized integration scheme with 112 directions.

The customized method is used to evaluate the integral Q of a function q on the surface of a revolution ellipsoid, with semi-major axis a and semi-minor axis b. Directions are located on the surface by the set of spherical coordinates (u, v) (Fig. 3-A). By virtue of the first fundamental form in differential geometry (Weisstein, 1999), the infinitesimal ellipsoid surface element is defined as: $dS = \sqrt{a^2 - (a^2 - b^2)\sin^2 u}\; dudv$. The integral Q then becomes:

$$Q(u,v) = \int_{u=0}^{\pi} \int_{v=0}^{2\pi} q(u,v) \sqrt{a^2 - (a^2 - b^2)\sin^2 u}\; dudv \tag{19}$$

Spheroid surface is discretized with a tiling using nine-nodes quadrangles (Fig. 3-B-C). The discretization is used as the integration basis for the function q, approximated with quadratic Lagrange polynomials for each quadrangle.

$$q(u,v) = \sum_{i,j=0}^{2} \alpha_{ij} u^i v^j \tag{20}$$

For each quadrangle I, q is evaluated on the nine nodes of I (Fig. 3-C) as q_i $(i = 1...9)$, with node

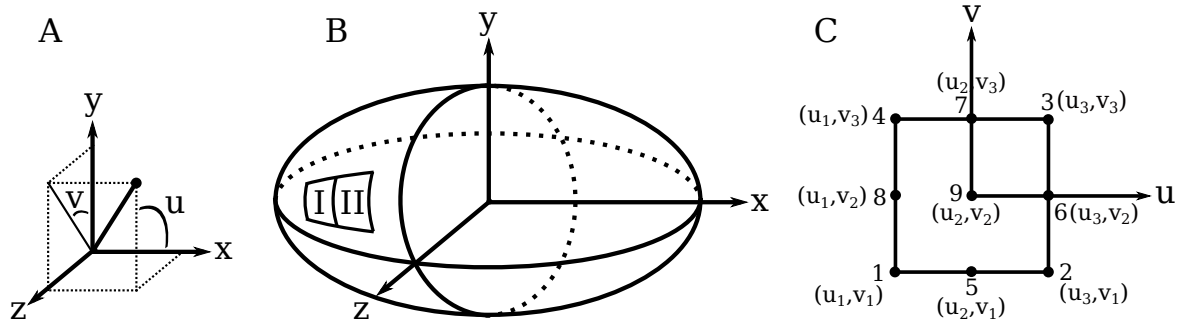

Figure 3: Numerical integration scheme: (A)-spherical angles defined in Cartesian basis, (B)-quadrangles tiling of the ellipsoid and (C)-representation of the nine-nodes quadrangle in the (u, v) space.

coordinates, providing an analytical expression of the coefficients α_{ij} of the Lagrange polynomials, only related to nodes and q_i by reversing the following system:

$$\begin{cases} q_1 = \sum_{i,j=0}^{2} \alpha_{ij}\ u_1^i v_1^j \\ q_2 = \sum_{i,j=0}^{2} \alpha_{ij}\ u_3^i v_1^j \\ q_3 = \sum_{i,j=0}^{2} \alpha_{ij}\ u_3^i v_3^j \\ q_4 = \sum_{i,j=0}^{2} \alpha_{ij}\ u_1^i v_3^j \\ q_5 = \sum_{i,j=0}^{2} \alpha_{ij}\ u_2^i v_1^j \\ q_6 = \sum_{i,j=0}^{2} \alpha_{ij}\ u_3^i v_2^j \\ q_7 = \sum_{i,j=0}^{2} \alpha_{ij}\ u_2^i v_3^j \\ q_8 = \sum_{i,j=0}^{2} \alpha_{ij}\ u_1^i v_2^j \\ q_9 = \sum_{i,j=0}^{2} \alpha_{ij}\ u_2^i v_2^j \end{cases} \tag{21}$$

Because of the size of the expressions, coefficients details are not shown. The coefficients α_{ij} are then included into the expression of q (Eq. (20)), expressed only with nodes parameters q_i $(i = 1...9)$ and u_j, v_j $(j = 1...3)$. The function q is integrated on each basis element X of the ellipsoid to evaluate the integral Q^X and the relative contributions of the element to the associated nodes $(A...I)^X$. To determine a node contribution, we consider a function q equal to 1 on this node and 0 on all the other nodes of the element. For the first quadrangle I, the integral is expressed as:

$$\begin{aligned} Q^I &= \int_{u_1}^{u_3} \int_{v_1}^{v_3} q(u,v) \sqrt{a^2 - (a^2 - b^2)\sin^2 u}\ du dv \\ &= A^I q_1 + B^I q_2 + C^I q_3 + D^I q_4 + E^I q_5 + F^I q_6 + G^I q_7 + H^I q_8 + I^I q_9 \end{aligned} \tag{22}$$

with A^I, B^I, C^I, D^I, E^I, F^I, G^I, H^I et I^I, only expressed with nodes coordinates u_i and v_i $(i = 1...3)$. For the second quadrangle II, the integral is expressed with nodes coordinates u_i $(i = 3...5)$ and v_j $(j = 1...3)$:

$$Q^{II} = A^{II} q_2 + B^{II} q_{10} + C^{II} q_{11} + D^{II} q_3 + E^{II} q_{12} + F^{II} q_{13} + G^{II} q_{14} + H^{II} q_6 + I^{II} q_{15} \tag{23}$$

The integration weights of each node are obtained by assembling elements, in the context of finite elements. Node weight ω is the summation of the contributions of every element in which the node is implicated as:

$$\omega = \begin{cases} \text{node } 1 : A^I + ... \\ \text{node } 2 : B^I + A^{II} ... \\ \text{node } 3 : C^I + B^{II} ... \\ \text{node } 4 : D^I + ... \\ \text{node } 5 : E^I + ... \\ \text{node } 6 : F^I + H^{II} + ... \\ ... \end{cases} \tag{24}$$

The integral Q can then be written, for a set of M directions $\underline{u_i}$, with M integration weights ω_i:

$$Q(u,v) = \sum_{i=0}^{M} \omega_i q(\underline{u_i}) \tag{25}$$

In order to verify the relevance of numerical integration, a non-linear function, $f(x) = e^x$, is integrated on the surface of different revolution ellipsoids, i) the unit sphere ($S_{R=1}$), ii) an ellipsoid with an axis ratio equals to 0.5 ($S_{R=0.5}$) and a degenerated ellipsoid with an axis ratio equals to 0.01 ($S_{R=0.01}$), with four numerical integration schemes based on:

- Bažant and Oh (1986)'s 122 directions network. The spherical network is deformed in ellipsoid and integration weights from the unit sphere are used.
- Bažant and Oh (1986)'s 122 directions network. The spherical network is conserved and integration weights from the unit sphere are penalized according to ellipsoidal geodesic.
- a network of 112 directions with numerical integration, previously defined in the present paper.
- a network of 422 directions with numerical integration, previously defined in the present paper.

In the first Bazant case, the anisotropy is taken into account on the deformations, as in the approach developed in the present paper while in the second Bazant case, anisotropy is taken into account on stresses, as in the micro-sphere approach. The results are compared with numerical integration computed with Scipy python library, using Gauss-Kronrod quadrature formula (Kronrod, 1965). Numerical results, longer to assess (10 times longer than an unoptimized straightforward implementation of the presented method) and therefore not usable in optimization or finite element simulation codes, are considered accurate and used as a basis for comparison on Table 1 which provides the relative errors between the different methods.

	$S_{R=1}$	$S_{R=0.5}$	$S_{R=0.01}$
Bazant (directions penalization)	$1.10^{-6}\%$	4.8%	7.9%
Bazant (weights penalization)	$1.10^{-6}\%$	5.2%	32%
Proposed method (112 directions)	$2.10^{-3}\%$	$2.10^{-3}\%$	$3.10^{-3}\%$
Proposed method (422 directions)	$2.10^{-4}\%$	$3.10^{-4}\%$	$3.10^{-4}\%$

Table 1: Relative error for numerical integration over a sphere, an ellipsoid with an axis ratio of 0.5 and an ellipsoid with an axis ratio of 0.01 with four methods.

For the integration on the surface of a sphere, Bažant and Oh (1986) method is the most efficient, with a relative error close to $10^{-6}\%$. Penalization has no effect whatsoever. However, the error becomes very large, multiplied by several million, when integrating on the surface of an ellipsoid. For a very thin ellipsoid, the error is almost 8% when ellipsoid directions are considered and 32% when spherical integration weights are penalized. With the method described in the present paper, the error remains constant and

weak whatever the shape of the surface to be integrated. Integration is thus objective. By increasing the number of directions, the relative error could be reduced. A compromise must therefore be chosen between computation time and precision. For the remainder of the study, the 422 directions network was chosen, considering the error insignificant.

With this numerical integration method, a random network of directions can be used or a specific network, coinciding with the structure of the material (Morch et al., 2019) for specific integrations. In addition, the surface element may be modified in a sufficiently direct way to achieve integration on any shape. Finally, the discretization according to anisotropy (Alastrué et al., 2009b) no longer requires significant refinement, thanks to the integration directly on the deformed network. For qualitative purposes, two methods are compared. Integration is first carried out on a spherical network with a penalty of rigidities (Fig. 4-A) as in microsphere models, then the network is deformed according to the geodesic of an ellipsoid, penalizing deformations (Fig. 4-B).

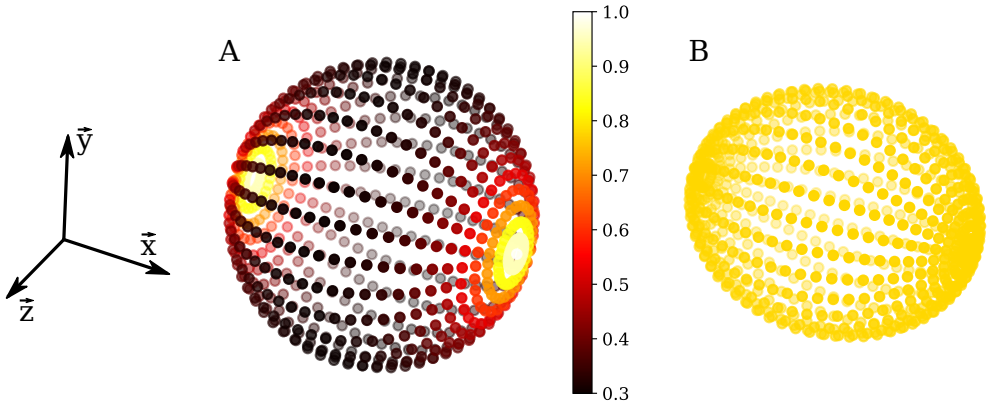

Figure 4: Integration points distribution for 874 directions: (A)-for a spherical network with a penalty on the rigidities according to the geodesic of an ellipsoid such as $R = 0.3$ and (B)-for an ellipsoidal network such as $R = 0.85$

An arbitrary material ($C = 5$ MPa, $N = 5$) whose anisotropy direction is set to $\theta = 0°$ and the anisotropy amplitude (related to ellipsoid axis ratio R) is chosen in order to obtain the same anisotropy ratio AR, *i.e.* the ratio between the stresses obtained for loading perpendicular to the anisotropy direction and for loading coincident with the anisotropy direction, is numerically tested. To obtain an AR in the range of 0.5, the spherical network is penalized with an ellipsoid with $R = 0.3$ and the ellipsoidal network is formed according to an ellipsoid with $R = 0.85$. To obtain an AR in the range of 0.3, the spherical network is penalized with an ellipsoid with $R = 0.02$ and the ellipsoidal network is formed according to an ellipsoid with $R = 0.75$. The study is also performed for a deformed network according to a degenerated ellipsoid with $R = 0.2$ to obtain an AR around 0.001. The stability of the AR is studied according to the number of integration directions, from 112 to 19184 in Fig 5 using as a reference the value obtained for 19184 directions.

As expected, when integrating over spherical networks, the accuracy decreases with the number of

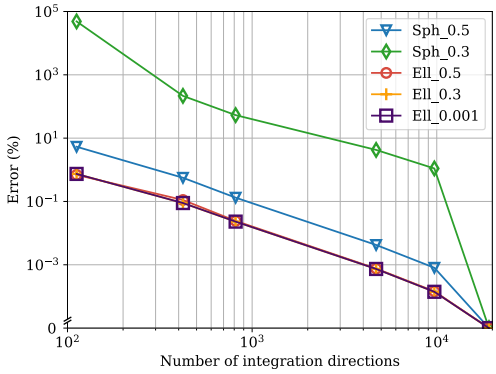

Figure 5: Variation of the anisotropy ratio AR error as a function of the number of integration directions obtained by integration over spherical networks penalized in rigidities (Sph_0.5,Sph_0.3) and ellipsoidal networks penalized in deformations (Ell_0.5,Ell_0.3,Ell_0.001). Each value is compared to the value obtained with the greatest number of directions (19184), considered as a reference.

integration points. In addition, this accuracy decreases rapidly with the increase in anisotropy. The higher the anisotropy, the more directions is needed. On the other hand, on ellipsoidal networks, the intensity of anisotropy does not affect accuracy. Regardless of the type of anisotropy, the values obtained are essentially the same. The number of directions can therefore remain constant for any case of anisotropy.

It should be noted that this integration method is subject to the same integration difficulties observed by Verron (2015) and Itskov (2016). A very large number of directions is required in case of multi-axial loading in very large deformation. The field of application is therefore limited to biological tissues where deformation rates are lower compared to synthetic polymers.

2.5. Model admissibility requirements

In order to be able to use the model to identify mechanical parameters, it is necessary to verify the thermodynamically eligibility of the model. As an illustration, an arbitrary numerical sample is selected with moderate anisotropy oriented (if not specified) along $\underline{x}$ axis: $R = 0.5$, $\theta = 0°$, $C = 5$ MPa and $N = 5$.

One of the main concerns in the constitutive modeling of materials is the validation of material frame indifference principle. Load responses must be unaffected by the rotation of the reference or material. To verify model objectivity, the example sample is rotated around $\underline{z}$ axis: the main orientation of the fibers varies accordingly. Loading is applied to the main direction of anisotropy, to the apex of the ellipsoid. Stress-stretch responses are shown in Fig. 6-A. Curves are superimposed with a relative error (RE) of $10^{-9}\%$ and are considered therefore equal, confirming rotation invariance. The same sample, oriented along $\underline{x}$ axis is also charged with two symmetrical loads ($+\pi/4$ and $-\pi/4$). Stress-stretch responses are plotted in Fig. 6-B. Symmetrical responses are strictly equal with a RE of $10^{-11}\%$, confirming model objectivity. Then, the constitutive laws do not depend on the external frame of reference used to describe them.

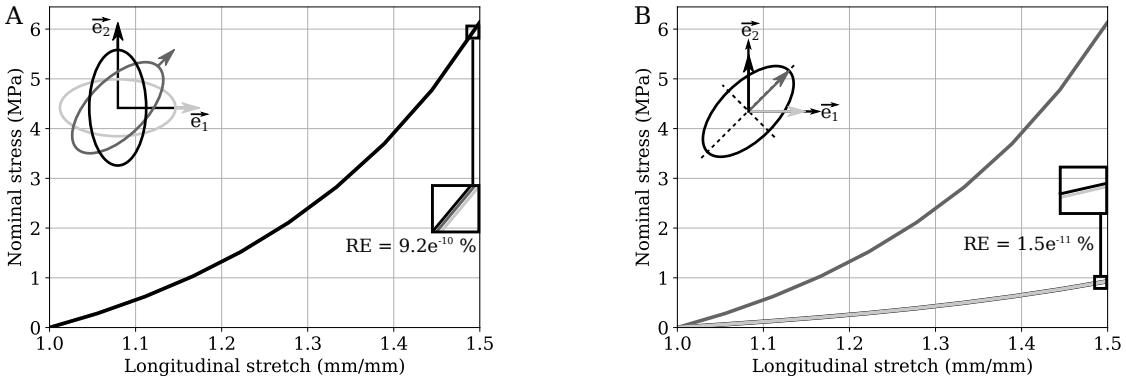

Figure 6: Influence of material rotation, nominal stress τ_{11} vs longitudinal stretch F_{11} responses of : (A)-3 different anisotropic materials with loadings in the main anisotropy orientation and (B)-an anisotropic material with 3 loadings including 2 symmetrical loads with respect to the anisotropy axis, with 422 directions integration scheme.

Moreover, in the context of hyperelastic problems, the polyconvexity of the strain energy density is a sufficient condition for the existence of the solution (Hill, 1956; Ball, 1976). The values of the strain energy density with its first and second derivatives with respect to the stretch are always positive and increasing, as observed in Fig. 7, meaning that the proposed density is an increasing monotonic function and is polyconvex with respect to its argument. Thus, the strain energy density satisfies the polyconvexity condition and guarantees the existence of a single solution. The material stability of the proposed model is therefore established.

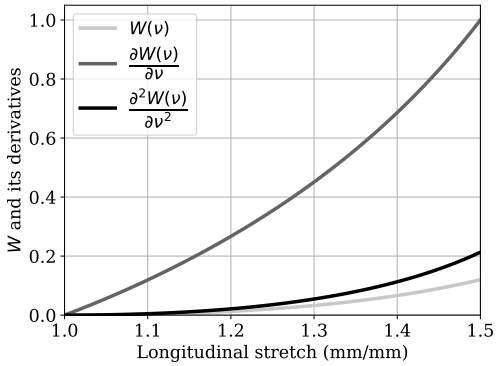

Figure 7: Strain energy density and its first and second derivatives according to ν with respect to longitudinal stretch F_{11}. For comparative purposes, the curves have been normalized, the shape remains unchanged.

In order to verify thermodynamic admissibility and convexity, the equivalent elasticity stiffness tensor $\mathbb{C}$ can be determined as:

$$\mathbb{C} = \frac{\partial \boldsymbol{S'}}{\partial \boldsymbol{E}} = \frac{4C}{\mathcal{S}} \iint_{\mathcal{S}} \beta \left(\frac{\sqrt{N}}{2} + \frac{(\nu - 1)\,\beta \sinh(\beta)^2}{\sinh(\beta)^2 - \beta^2} \right) ((\underline{u} \otimes \underline{u}) \otimes (\underline{u} \otimes \underline{u}))\ d\mathcal{S} \tag{26}$$

with $\beta = \mathcal{L}^{-1}\left(\frac{\nu}{\sqrt{N}}\right)$. The fourth-rank tensor may be written in 2-index Mandel notation as the matrix:

$$\mathbb{C} = \begin{bmatrix} C_{1111} & C_{1122} & C_{1133} & \sqrt{2}C_{1123} & \sqrt{2}C_{1131} & \sqrt{2}C_{1112} \\ C_{2211} & C_{2222} & C_{2233} & \sqrt{2}C_{2223} & \sqrt{2}C_{2231} & \sqrt{2}C_{2212} \\ C_{3311} & C_{3322} & C_{3333} & \sqrt{2}C_{3323} & \sqrt{2}C_{3331} & \sqrt{2}C_{3312} \\ \sqrt{2}C_{2311} & \sqrt{2}C_{2322} & \sqrt{2}C_{2333} & 2C_{2323} & 2C_{2331} & 2C_{2312} \\ \sqrt{2}C_{3111} & \sqrt{2}C_{3122} & \sqrt{2}C_{3133} & 2C_{3123} & 2C_{3131} & 2C_{3112} \\ \sqrt{2}C_{1211} & \sqrt{2}C_{1222} & \sqrt{2}C_{1233} & 2C_{1223} & 2C_{1231} & 2C_{1212} \end{bmatrix} \tag{27}$$

Whatever the state of deformation applied and the type of sample, this matrix becomes:

$$\mathbb{C} = \begin{bmatrix} C_{11} & C_{12} & C_{12} & 0 & 0 & 0 \\ C_{12} & C_{22} & C_{23} & 0 & 0 & 0 \\ C_{12} & C_{23} & C_{22} & 0 & 0 & 0 \\ 0 & 0 & 0 & C_{22} - C_{23} & 0 & 0 \\ 0 & 0 & 0 & 0 & 2C_{55} & 0 \\ 0 & 0 & 0 & 0 & 0 & 2C_{55} \end{bmatrix} \tag{28}$$

The shape of $\mathbb{C}$ is consistent with the transverse isotropy hypothesis. To verify the polyconvexity hypothesis, it is sufficient that $\mathbb{C}$ is defined as positive regardless of the state of deformation applied. The diagonalization of the matrix shows that the terms are always positive and increasing. Moreover, during the loading phase, the coefficients C_{ij} exhibit a convex evolution.

The thermodynamic admissibility hypothesis leads also to restrictions on the elastic coefficients of $\mathbb{C}$. Through the generalized Hooke's law, the Young moduli and Poisson ratios verify Lempriere (1968) inequalities and thus ensure the existence and admissibility of the micro-ellipsoid model.

3. Theoretical results of the proposed model

In order to verify its relevance and consistency, the proposed model is applied to numerical uni-axial tensile tests performed in various directions of loadings on specimen from:

- Isotropic sample with evenly distributed fibers (Fig. 8-A)
- Anisotropic sample with a broad fibers distribution (moderate anisotropy) centered on θ (Fig. 8-B)
- Anisotropic sample with highly oriented fibers (huge anisotropy) at θ (Fig. 8-C)

It is assumed that samples are transversely isotropic. For an isotropic sample, the fibers distribution is homogeneous, so the ratio between major and minor ellipsoid axis, R, equals 1. The anisotropy thus can be defined as: $A = 1 - R$. When anisotropy is increasing ($A > 0$), ratio R is decreasing ($R < 1$).

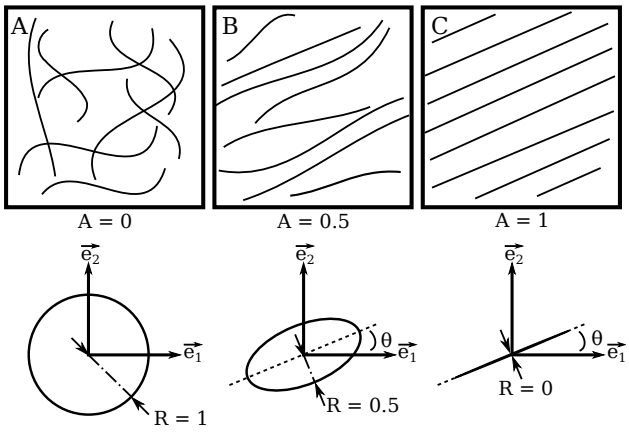

Figure 8: Examples of numerical samples with three types of anisotropy and the associated ellipsoid of orientation distribution: (A)-isotropic with a spherical distribution, (B)-moderately anisotropic with a large ellipsoidal distribution and (C)-very anisotropic with a thin ellipsoidal distribution.

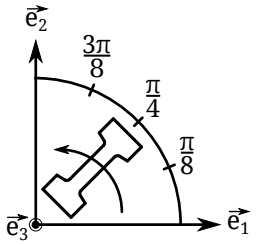

Figure 9: Loads applied on the specimens between 0 and $\frac{\pi}{2}$, in the sample reference $(\underline{e_1}, \underline{e_2}, \underline{e_3})$.

Five types of loading between 0 and $\pi/2$ (Fig. 9) are simulated on every sample and the main orientation θ of the anisotropy is chosen at $\pi/8$ from the sample basis $(\underline{e_1}, \underline{e_2}, \underline{e_3})$. The material parameters, C and N are arbitrarily fixed as: $C = 5MPa$ and $N = 5$ (dimensionless), constant whatever the type of anisotropy and the direction $\underline{u}_i$. Stresses are assessed with the nominal stress tensor from the Eq. (9), (12), (18) and (25):

$$\boldsymbol{\tau} = C\sqrt{N} \sum_{i=0}^{M=422} \omega_i \sqrt{\nu_i - 1}\, \mathcal{L}^{-1}\left(\frac{\nu_i}{\sqrt{N}}\right) \boldsymbol{F}(\underline{u}_i \otimes \underline{u}_i) - p\boldsymbol{F}^{-T} \tag{29}$$

3.1. Isotropic case

The directional model is applied on numerical isotropic sample and five loading directions are simulated with a stretch of 1.5. Thank to the sample isotropy, fibers and therefore mechanical properties are evenly distributed over space, the integration is over a sphere with $R = 1$. The ellipsoid deforms the initial lengths of the fibers, so for a sphere the fibers are equivalent in every directions, with strictly equal mechanical and structural properties. The first Piola-Kirchhoff stress tensor $\boldsymbol{\tau}$ and the transformation gradient tensor $\boldsymbol{F}$ are evaluated in the principal stresses reference $(\underline{e_{\sigma I}}, \underline{e_{\sigma II}}, \underline{e_{\sigma III}})$, the loading reference (Eq. (14)). Stretch-stress

responses are shown on the Fig. 10. Nominal stresses τ_{11} for each loading are plotted with respect to the longitudinal strain (F_{11}). As expected for an isotropic sample, all curves are superimposed. Strain responses are equal whatever the loading direction. To quantify the integration error, the relative error (RE) is calculated as the largest difference between curves for the last acquired stretch. Here, the RE is 0.18%, considered as insignificant. The model applied to an isotropic sample returns a perfectly isotropic response, regardless the load.

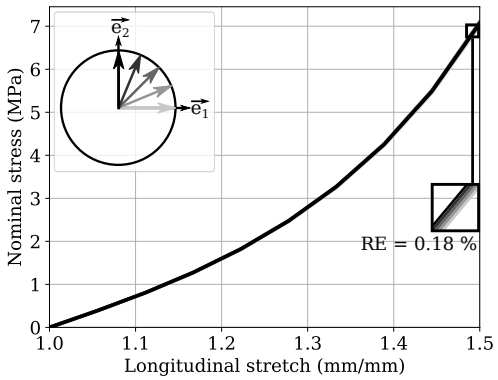

Figure 10: Nominal stress τ_{11} vs longitudinal stretch F_{11} responses for an isotropic sample along 5 directions of loadings.

3.2. Moderately anisotropic case

The five loading directions are now simulated with the same stretch of 1.5 on a moderately anisotropic sample (Fig. 8-B). Because of the sample anisotropy, fibers and therefore structural properties are not equal with directions. The ellipsoid deforms, according to its geodesic, the initial lengths of the fibers, then modifying the mechanical responses according to the direction of loading. Anisotropy A is evaluated to 0.5, minor axis R equals $1 - A = 0.5$. The anisotropy main orientation is set to $\pi/8$. The model is then integrated on the surface of an ellipsoid with a minor axis R and oriented at $\pi/8$. Stress-stretch responses are shown in Fig. 11. Loadings at 0 and $\pi/4$ are therefore symmetrical, as illustrated on the figure: curves are superimposed, with a RE of 10^{-8}%. This superposition of the responses is due to the symmetry of the load with respect to the main orientation of the anisotropy. The others loading directions are well ordered: the loading at $\pi/8$, corresponding to the main anisotropy direction, is the stiffest. The shape of the ellipsoid represents the spatial distribution of fibers. The direction at $\pi/2$ corresponds to the least dense loaded sample direction. At $\pi/2$, there are therefore fewer fibers than at $\pi/8$. Its response is consequently the least rigid. To characterize the anisotropy level, the anisotropy ratio (AR) between the last acquired stresses (corresponding to a stretch of 1.5) for a loading at $(\pi/8 + \pi/2)$ and a loading at $\pi/8$ is evaluated:

$$AR = \left. \frac{\sigma(\theta + \pi/2)}{\sigma(\theta)} \right|_{\lambda=1.5}$$

A loading in the main direction of anisotropy has a response 16 times stiffer than a loading in a perpendicular direction, corresponding to $AR = 0.063$.

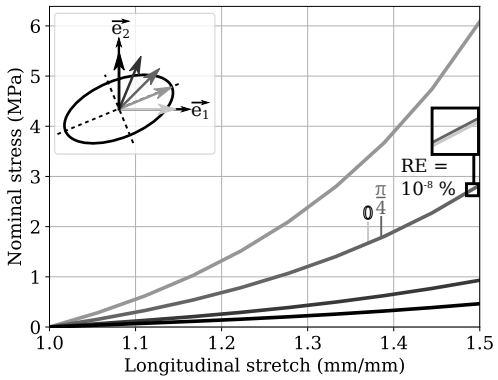

Figure 11: Nominal stress τ_{11} vs longitudinal stretch F_{11} responses for an anisotropic sample with a moderate anisotropy along 5 directions of loadings.

3.3. Highly anisotropic case

The simulation is performed on the highly anisotropic sample, in five loading directions and a stretch of 1.5. The anisotropy is set to 0.9 (an anisotropy set to 1 is ideal but unable to be simulated), which corresponds to an ellipsoid with a minor axis at 0.1. The model is then integrated on the surface of an ellipsoid with a minor axis equals to 0.1 and oriented at $\pi/8$. Stress-stretch responses are shown in Fig. 12. The predominant direction, at $\pi/8$, is very far from the others, because of the very strong anisotropy of the sample. A very thin ellipsoid implies a near absence of fibers in the other directions, which gives near zero stress responses. Loadings at 0 and $\frac{\pi}{4}$ responses are superimposed, with a RE of $10^{-9}\%$. Here, the AR is close to 0.000125, which would never corresponds to our biologic tissue behavior. The model can therefore be use in its operational range.

4. Application to human abdominal rectus sheath

The anisotropic constitutive model presented in this article is consistent and reflective of the anisotropic behaviour of the numerical tissues tested. However, it is interesting to evaluate this model against experimental results in order to test its validity.

This microstructure-based model is developed with the main assumptions that structural parameters and material parameters can be decoupled and that structural parameters play a significant role for classical range of material characteristics. To verify the validity of this hypothesis, model is applied to human abdominal wall connective tissue. Connective tissues are composites with an interweaving of collagen and elastin fibers, leading to highly anisotropic behavior due to their oriented microstructure (Korenkov et al.,

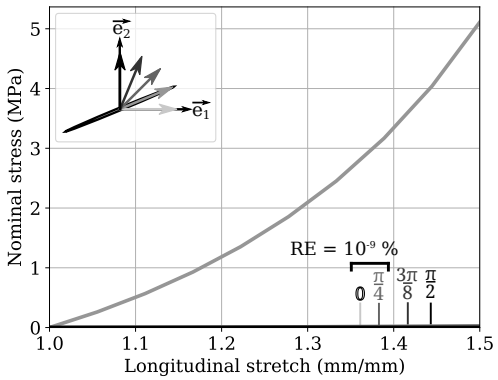

Figure 12: Nominal stress τ_{11} vs longitudinal stretch F_{11} responses for an anisotropic sample with a huge anisotropy along 5 directions of loadings

2001; Gasser et al., 2006). The model is parameterized using a set of micro-structural parameters derived from fibers distribution (A,θ) and a set of mechanical parameters related to macromolecules (C,N). First, structural parameters are imposed in order to identify the material parameters on one experimental data set. In a second step, the structural parameters are identified using the precedent identified material parameters and compared to real parameters. The quality of the fittings are evaluated by computing the coefficient of determination R^2.

In the present paper, from two different individuals, epigastric anterior rectus sheath were sampled (Astruc et al., 2018). From each sample, three specimens were retrieved very close to each others to asssume the fibers orientations are equivalent. Then each sample was tested under uni-axial tension along three directions of loading. Tests were performed under a multi-photon confocal microscope (Levillain et al., 2016). The three-dimensional collagen images acquired with the microscope were then processed by texture analysis (Rao and Schunck, 1991; Westin et al., 2002) to obtain a distribution of fibers orientations, represented as an ellipsoid (Fig. 1). The anisotropy of the collagen fibers were therefore included through an ellipsoid oriented in the main direction and whose minor axis corresponds to the dispersion of the fibers.

4.1. Identification of material parameters

The first individual is used to obtain material parameters (C,N). A classical multi-photon confocal image is given in Fig. 13-A where collagen fibers are clearly visible in red. Texture image analysis provides micro-structural information about the anisotropy with a main orientation of the fibers, θ close to 31°, and the minor axis of the anisotropy ellipsoid, R close to 0.20. Experimental stress-stretch curves obtained in the three loading directions (0°, 45° and 90°) are given in Fig. 13-B in dashed lines. The optimization of the material parameters is obtained through the minimization of the error between the experimental and modeled curves along the three directions, using a Truncated-Newton algorithm (Dembo and Steihaug, 1983), available in Python library Scipy (Jones et al., 2001). The material parameters, C and N, for collagen

fibers are given in Table 2:

Identified material parameters	
C (MPa)	23.1
N	11.3

Table 2: Identified material parameters (intrinsic) for the first individual rectus sheath samples based on comparison between nominal stress-stretch curves in the three loading directions.

The optimization of the directional model is close to the experimental data. With a single pair of identified parameters, the three stress-stretch responses are modeled, showing a good agreement of the numerical results (solid line) with the experimental data (Fig. 13-B), with R^2 close to 1. Moreover, the identified parameters are consistent with the results of Brieu et al. (2016) for collagen fibers, namely $C_C = 4.7$MPa and $N_C = 21.1$, with similar orders of magnitude. The chain density n, derived from the rigidity $C = n\kappa_B T$, as $n = 5.6e^{21}m^{-3}$, is also consistent with the density used in Kuhl et al. (2006) study for tendon collagen soft tissues, $\gamma_{ch} = 7e^{21}m^{-3}$. Elastic moduli of biological tissues are generally lower: in a previous study on connective tissues of the abdominal wall (Astruc et al., 2018), the moduli ranged from 0.39 MPa in small deformations to 15 MPa in large deformations. However, in this constitutive model, the C parameter does not correspond to the stiffness of the entire tissue, but to the stiffness of the unit element, the fiber. Sherman et al. (2015) conducted a literature review on collagen tissues at different scales. The rigidity of the collagen molecule is in the GPa range while the whole tissue has a modulus in the MPa range, or even kPa. Sasaki and Odajima (1996) explains this phenomenon by the organization of collagen fibers that are not directly recruited in traction. The apparent rigidity of the entire tissue therefore appears to be reduced. The parameter determined by the optimization is therefore consistent.

4.2. Identification of structural parameters

For the second individual, the microscopic observations of collagen fibers using confocal microscopy are given in Fig. 14-A. Texture image analysis provides micro-structural information about the anisotropy with a main orientation of the fibres, θ, close to 12°, and the minor axis of the anisotropy ellipsoid, R close to 0.13. As in the study by (Brieu et al., 2016), the mechanical parameters of the collagen fibers of the rectus sheath are considered similar for each non-pathological individual. The only varying information is the microstructure, described thorough the spatial arrangement of the fibers. The identified material parameters, $C = 23.1$MPa and $N = 11.3$, obtained from the first individual are then used as inputs for the second individual. Fig. 14-B gives the experimental (dashed line) of the stress-stretch curves for the second individuals rectus sheath samples and the results of numerical simulation (continuous line) with $\theta = 12°$, $R = 0.13$, $C = 23.1$MPA and $N = 11.3$ for the three loading directions. Numerical and experimental

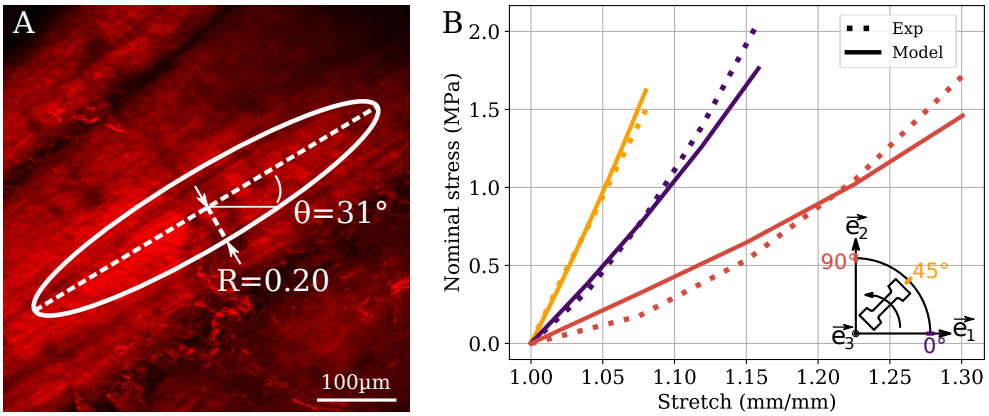

Figure 13: (A)-Microscopic observations of collagen fibers with the related anisotropy ellipsoid and (B)-comparison of experimental (dashed line) and modeled (continuous line) stress-stretch responses for three directions of loading for the first individual rectus sheath samples using the identified material parameters $C = 23.1$MPa and $N = 11.3$. The quality of each fitting is evaluated with: $R^2_{45°} = 0.99$, $R^2_{0°} = 0.96$, $R^2_{90°} = 0.94$.

responses are close, validating the hypothesis that the properties of materials are not specific to individuals. Material properties are constant and independent of the individuals.

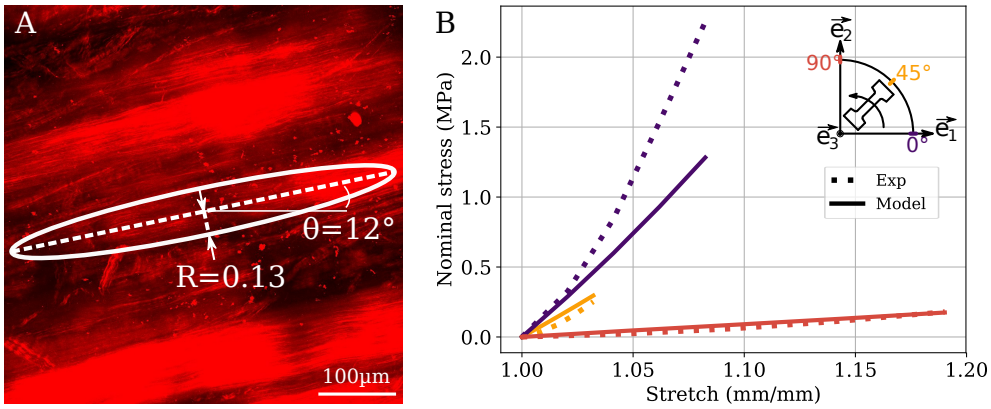

Figure 14: (A)-Microscopic observations of collagen fibers with the related anisotropy ellipsoid and (B)-comparison of experimental (dashed line) and modeled (continuous line) stress-stretch responses for three directions of loading for the second individual rectus sheath samples using the fixed material parameters, $C = 23.1$MPa and $N = 11.3$. The quality of each fitting is evaluated with: $R^2_{45°} = 0.76$, $R^2_{0°} = 0.60$, $R^2_{90°} = 0.92$.

Conversely, a reverse procedure can be performed to identify the structural parameters related to the microstructure, based on the experimental stress-stretch curves of the second individual with the fixed material parameters $C = 23.1$MPa and $N = 11.3$, with no mention about anisotropy. Then, the identified parameters obtained using the Truncated-Newton algorithm are the main orientation of fibers, θ, and the ellipsoid minor axis, R given in Table 3:

Identified structural parameters	
θ (°)	10
R	0.14

Table 3: Identified structural parameters (extrinsic) for the second individual rectus sheath samples based on comparison between nominal stress-strech curves in the three loading directions samples using the fixed material parameters $C = 23.1$ MPa and $N = 11.3$.

The numerical responses (solid lines) are close to the experimental data (dashed lines), as observed in Fig. 15. With the fixed material parameters and the identified pair of structural parameters, the three stress stretch responses are modeled, showing a good agreement between the numerical results and the experimental data. Identified structural parameters are then successfully compared to the microscopic observations (Fig. 14-A). The experimental main orientation is 12°, close to the identified value, just as for the experimental ellipsoid minor axis, set at 0.13. These parameters are completely consistent with the identified values, validating the similarity hypothesis of macromolecular properties. With material parameters C and N set, the only needed information to predict behavior is structural.

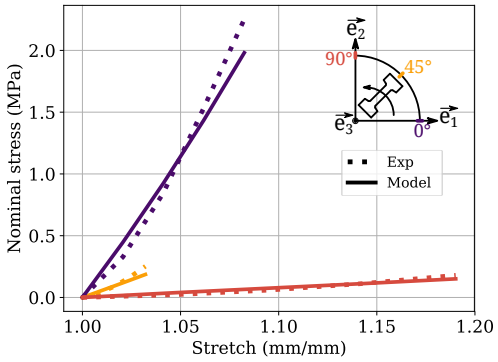

Figure 15: Comparison of experimental (dashed line) and modeled (continuous line) stress-stretch responses for three directions of loading for the second individual rectus sheath samples using the fixed material parameters $C = 23.1$MPa and $N = 11.3$ and the identified structural parameters $\theta = 10°$ and $R = 0.14$. The quality of each fitting is evaluated with: $R^2_{45°} = 0.91$, $R^2_{0°} = 0.76$, $R^2_{90°} = 0.94$.

5. Conclusion

In this paper, based on the microstructural description of the tissues, we have proposed a constitutive model accounting the anisotropic and non-linear behavior of fibrous biological tissues, without prior knowledge of the nature of anisotropy. The originality of this model lies in its consideration of anisotropy. Instead of penalizing rigidities as in conventional models, anisotropy is taken into account on the initial lengths

of the fibers, thus impacting only the structural (or extrinsic) parameters of the fibers. The material (or intrinsic) parameters are then considered similar for any individual. The only variables are the structural parameters, related to the architecture of the tissue. Moreover modeling the impact of anisotropy by penalizing deformations rather than stresses prevents prevents the solution obtained by our numerical integration scheme from being degraded when the amplitude of anisotropy is increased.

The model was tested on three numerical examples. Its consistency and invariance have been proved. The model was then applied to several biological tissue tests. The intrinsic parameters could be determined based on the histological description of the first set of tests and applied to the second set of tests. The extrinsic parameters, corresponding to the anisotropy of the tissue could then be predicted, showing a good adequacy with the experimental tests.

Non-linear anisotropic behavior can therefore be predicted with a microscopic description of tissues, considering that the parameters of the constitutive fibers are similar for every individuals. Extrinsic parameters, relative to the structure, and intrinsic parameters, relative to the material, are fully decoupled. Knowing the material parameters of the fibers, it is then sufficient to feed the model with microscopic observations to predict the behaviour of anisotropic fibrous tissues.

This model will be implemented in further studies a in finite element code to describe more complex structures such as the abdominal wall. In the long term, the mechanical behaviour of tissues could then be fully understood and would lead to patient-specific simulations, to guide the improvement of medical treatments.

Acknowledgement

We would like to thank Medtronic and the IVTV ANR-10-EQPX-06-01 for their financial support. We also wish to thank Thomas Helfer (CEA, France) for his insightful comments.

References

Abraham, A. C., Moyer, J. T., Villegas, D. F., Odegard, G. M., Haut Donahue, T. L., feb 2011. Hyperelastic properties of human meniscal attachments. Journal of biomechanics 44 (3), 413–418.

Alastrué, V., Martínez, M. A., Doblaré, M., Menzel, A., 2009a. Anisotropic micro-sphere-based finite elasticity applied to blood vessel modelling. Journal of the Mechanics and Physics of Solids 57 (1), 178–203.

Alastrué, V., Martinez, M. A., Menzel, A., Doblaré, M., 2009b. On the use of non-linear transformations for the evaluation of anisotropic rotationally symmetric directional integrals. Application to the stress analysis in fibred soft tissues. International Journal for Numerical Methods in Engineering 79, 474–504.

Alastrué, V., Sáez, P., Martínez, M. A., Doblaré, M., 2010. On the use of the Bingham statistical distribution in microsphere-based constitutive models for arterial tissue. Mechanics Research Communications 37 (8), 700–706.

Arruda, E. M., Boyce, M. C., 1993. A three-dimensional constitutive model for the large stretch behavior of rubber elastic materials. Journal of the Mechanics and Physics of Solids 41 (2), 389–412.

Astruc, L., De Meulaere, M., Witz, J. F., Nováček, V., Turquier, F., Hoc, T., Brieu, M., 2018. Characterization of the anisotropic mechanical behavior of human abdominal wall connective tissues. Journal of the Mechanical Behavior of Biomedical Materials 82, 45–50.

Ball, J. M., 1976. Convexity Conditions and Existence Theorems in Nonlinear Elasticity. Archive of Rational Mechanics and Analysis 63, 337–403.

Bažant, P., Oh, B. H., 1986. Efficient Numerical Integration on the Surface of a Sphere. ZAMM Journal of Applied Mathematics and Mechanics / Zeitschrift für Angewandte Mathematik und Mechanik 66 (1), 37–49.

Bergonnier, S., Hild, F., Rieunier, J.-B., Roux, S., 2005. Strain heterogeneities and local anisotropy in crimped glass wool. Journal of materials science 40, 5949–5954.

Bingham, C., 1974. An Antipodally Symmetric Distribution on the Sphere. The Annals of Statistics 2 (6), 1201–1225.

Boubaker, M. B., Haboussi, M., Ganghoffer, J.-F., Aletti, P., 2015. Predictive model of the prostate motion in the context of radiotherapy: A biomechanical approach relying on urodynamic data and mechanical testing. Journal of the Mechanical Behavior of Biomedical Materials 49, 30–42.

Brieu, M., Chantereau, P., Gillibert, J., de Landsheere, L., Lecomte, P., Cosson, M., 2016. A nonlinear-elastic constitutive model for soft connective tissue based on a histologic description: Application to female pelvic soft tissue. Journal of the Mechanical Behavior of Biomedical Materials 58, 65–74.

Chagnon, G., Rebouah, M., Favier, D., 2015. Hyperelastic Energy Densities for Soft Biological Tissues: A Review. Journal of Elasticity 120 (2), 129–160.

Ciarletta, P., Izzo, I., Micera, S., Tendick, F., 2011. Stiffening by fiber reinforcement in soft materials: A hyperelastic theory at large strains and its application. Journal of the Mechanical Behavior of Biomedical Materials 4 (7), 1359–1368.

Cohen, A., 1991. A Padé approximant to the inverse Langevin function. Rheologica Acta 30 (3), 270–273.

Criscione, J. C., McCulloch, A. D., Hunter, W. C., 2002. Constitutive framework optimized for myocardium and other high-strain, laminar materials with one fiber family. Journal of the Mechanics and Physics of Solids 50 (8), 1681–1702.

Dembo, R. S., Steihaug, T., 1983. Truncated-newtono algorithms for large-scale unconstrained optimization. Mathematical Programming 26 (2), 190–212.

Diani, J., Brieu, M., Vacherand, J. M., 2006. A damage directional constitutive model for Mullins effect with permanent set and induced anisotropy. European Journal of Mechanics, A/Solids 25 (3), 483–496.

Diani, J., Brieu, M., Vacherand, J. M., Rezgui, A., 2004. Directional model for isotropic and anisotropic hyperelastic rubber-like materials. Mechanics of Materials 36 (4), 313–321.

Gasser, T. C., Ogden, R. W., Holzapfel, G. A., 2006. Hyperelastic modelling of arterial layers with distributed collagen fibre orientations. Journal of the Royal Society Interface 3 (6), 15–35.

Gillibert, J., Brieu, M., Diani, J., 2010. Anisotropy of direction-based constitutive models for rubber-like materials. International Journal of Solids and Structures 47 (5), 640–646.

Göktepe, S., Miehe, C., 2005. A micro-macro approach to rubber-like materials. Part III: The micro-sphere model of anisotropic Mullins-type damage. Journal of the Mechanics and Physics of Solids 53 (10), 2259–2283.

Gräßel, D., Prescher, A., Fitzek, S., Keyserlingk, D. G. V., Axer, H., 2005. Anisotropy of human linea alba: A biomechanical study. Journal of Surgical Research 124 (1), 118–125.

Guérin, G., Turquier, F., 2013. Impact of the defect size, the mesh overlap and the fixation depth on ventral hernia repairs: A combined experimental and numerical approach. Hernia 17 (5), 647–655.

Heo, S., Xu, Y., 2001. Constructing fully symmetric cubature formulae for the sphere. Mathematics of computation 70 (233), 269–279.

Hill, R., 1956. New horizons in the mechanics of solids. Journal of the Mechanics and Physics of Solids 5 (1), 66–74.

Holzapfel, G. A., Niestrawska, J. A., Ogden, R. W., Reinisch, A. J., Schriefl, A. J., 2015. Modelling non-symmetric collagen

fibre dispersion in arterial walls. Journal of the Royal Society Interface 12 (20150188).

Hostettler, A., George, D., Rémond, Y., Nicolau, S. A., Soler, L., Marescaux, J., 2010. Bulk modulus and volume variation measurement of the liver and the kidneys in vivo using abdominal kinetics during free breathing. Computer Methods and Programs in Biomedicine 100 (2), 149–157.

Itskov, M., May 2016. On the accuracy of numerical integration over the unit sphere applied to full network models. Computational Mechanics 57 (5), 859–865.

Jedynak, R., 2015. Approximation of the inverse Langevin function revisited. Rheologica Acta 54, 29–39.

Jones, E., Oliphant, T., Peterson, P., et al., 2001. SciPy: Open source scientific tools for Python.
URL `http://www.scipy.org/`

Kaster, T., Sack, I., Samani, A., 2011. Measurement of the hyperelastic properties of ex vivo brain tissue slices. Journal of Biomechanics 44 (6), 1158–1163.

Knutsson, H., Westin, C.-f., Andersson, M., 2011. Representing Local Structure Using Tensors II. Lecture Notes in Computer Science, 545–556.

Korenkov, M., Beckers, A., Koebke, J., Lefering, R., Tiling, T., Troidl, H., 2001. Biomechanical and morphological types of the linea alba and its possible role in the pathogenesis of midline incisional hernia. European Journal of Surgery 167 (12), 909–914.

Krause, M., Hausherr, J. M., Burgeth, B., Herrmann, C., Krenkel, W., 2010. Determination of the fibre orientation in composites using the structure tensor and local X-ray transform. Journal of Materials Science · 45, 888–896.

Kronrod, A. S., 1965. Nodes and weights of quadrature formulas, sixteen-place tables: Authorized translation from the Russian.

Kuhl, E., Garikipati, K., Arruda, E. M., Grosh, K., 2005. Remodeling of biological tissue: Mechanically induced reorientation of a transversely isotropic chain network. Journal of the Mechanics and Physics of Solids 53 (7), 1552–1573.

Kuhl, E., Menzel, A., Garikipati, K., Arruda, E. M., Grosh, K., 2006. Modeling and Simulation of Remodeling in Soft Biological Tissues. Springer Berlin Heidelberg, Berlin, Heidelberg, pp. 77–89.

Kuhn, W., Grün, F., 1942. Beziehungen zwischen elastischen Konstanten und Dehnungsdoppelbrechung hochelastischer Stoffe. Kolloid-Zeitschrift 101 (3), 248–271.

Lapeer, R. J., Gasson, P. D., Karri, V., 2010. Simulating plastic surgery: From human skin tensile tests, through hyperelastic finite element models to real-time haptics. Progress in Biophysics and Molecular Biology 103 (2), 208–216.

Lempriere, B. M., nov 1968. Poisson's ratio in orthotropic materials. AIAA Journal 6 (11), 2226–2227.

Levillain, A., Orhant, M., Turquier, F., Hoc, T., 2016. Contribution of collagen and elastin fibers to the mechanical behavior of an abdominal connective tissue. Journal of the Mechanical Behavior of Biomedical Materials 61, 308–317.

Li, K., Ogden, R. W., Holzapfel, G. A., 2018. A discrete fibre dispersion method for excluding fibres under compression in the modelling of fibrous tissues. Journal of The Royal Society Interface 15 (138), 1–27.

Lister, K., Gao, Z., Desai, J. P., 2011. Development of in vivo constitutive models for liver: Application to surgical simulation. Annals of Biomedical Engineering 39 (3), 1060–1073.

Martins, P., Peña, E., Jorge, N. R., Santos, A., Santos, L., Mascarenhas, T., Calvo, B., 2012. Mechanical characterization and constitutive modelling of the damage process in rectus sheath. Journal of the Mechanical Behavior of Biomedical Materials 8, 111–122.

Mayeur, O., Jeanditgautier, E., Witz, J. F., Lecomte-Grosbras, P., Cosson, M., Rubod, C., Brieu, M., 2017. Evaluation of strains on levator ani muscle: damage induced during delivery for a prediction of patient risks. In: Springer, C. (Ed.), Computational Biomechanics for Medicine. pp. 135–146.

Merckel, Y., Diani, J., Brieu, M., Caillard, J., 2013. Constitutive modeling of the anisotropic behavior of Mullins softened filled rubbers. Mechanics of Materials 57, 30–41.

Miehe, C., Göktepe, S., Lulei, F., 2004. A micro-macro approach to rubber-like materials - Part I: The non-affine micro-sphere

model of rubber elasticity. Journal of the Mechanics and Physics of Solids 52 (11), 2617–2660.

Mooney, M., 1940. A theory of large elastic deformation. Journal of Applied Physics 11 (9), 582–592.

Morch, A., Astruc, L., Witz, J.-F., Lesaffre, F., Lecomte-Grosbras, P., Soulat, D., Brieu, M., 2019. Modeling of anisotropic hyperelastic heterogeneous knitted fabric reinforced composites. Journal of the Mechanics and Physics of Solids.

Ogden, R. W., 1978. Nearly isochoric elastic deformations: Application to rubberlike solids. Journal of the Mechanics and Physics of Solids 26 (1), 37–57.

Polzer, S., Gasser, T. C., Novak, K., Man, V., Tichy, M., Skacel, P., Bursa, J., 2015. Structure-based constitutive model can accurately predict planar biaxial properties of aortic wall tissue. Acta Biomaterialia 14, 133–145.

Rao, A. R., Schunck, B. G., 1991. Computing oriented texture fields. CVGIP: Graphical Models and Image Processing 53 (2), 157–185.

Rivlin, R. S., 1948. Large elastic deformations of istropic materials. IV. Further developments of the general theory. Philosophical Transactions of the Royal Society of London. Series A, Mathematical and Physical Sciences 241 (835), 379–397.

Sáez, P., García, A., Peña, E., Gasser, T. C., Martínez, M. A., 2016. Microstructural quantification of collagen fiber orientations and its integration in constitutive modeling of the porcine carotid artery. Acta Biomaterialia 33, 183–193.

Sasaki, N., Odajima, S., 1996. Elongation mechanism of collagen fibrils and force-strain relations of tendon at each level of structural hierarchy. Journal of Biomechanics 29 (9), 1131–1136.

Sherman, V. R., Yang, W., Meyers, M. A., 2015. The materials science of collagen. Journal of the Mechanical Behavior of Biomedical Materials 52, 22–50.

Silva, M. E. T., Brandão, S., Parente, M. P. L., Mascarenhas, T., Jorge, R. M. N., Brandão, S., Parente, M. P. L., Mascarenhas, T., Natal, R. M., 2017. Computer Methods in Biomechanics and Biomedical Engineering Biomechanical properties of the pelvic floor muscles of continent and incontinent women using an inverse finite element analysis. Computer Methods in Biomechanics and Biomedical Engineering 5842 (March), 0.

Spronck, B., Megens, R. T., Reesink, K. D., Delhaas, T., 2016. A method for three-dimensional quantification of vascular smooth muscle orientation: application in viable murine carotid arteries. Biomechanics and Modeling in Mechanobiology 15 (2), 419–432.

Treloar, L. R. G., Riding, G., 1979. A Non-Gaussian Theory for Rubber in Biaxial Strain. I. Mechanical Properties. Proceedings of the Royal Society A: Mathematical, Physical and Engineering Sciences 369 (1737), 261–280.

Verron, E., 2015. Questioning numerical integration methods for microsphere (and microplane) constitutive equations. Mechanics of Materials 89, 216–228.

Wang, M. C., Guth, E., 1952. Statistical theory of networks of non-gaussian flexible chains. The Journal of Chemical Physics 20 (7), 1144–1157.

Weisstein, E. W., 1999. First Fundamental Form. From MathWorld–A Wolfram Web Resource.
URL `http://mathworld.wolfram.com/FirstFundamentalForm.html`

Westin, C.-F., Maier, S. E., Mamata, H., Nabavi, A., Jolesz, F. A., Kikinis, R., 2002. Processing and visualization for diffusion tensor MRI. Medical Image Analysis 6 (2), 93–108.

Wex, C., Arndt, S., Stoll, A., Bruns, C., Kupriyanova, Y., 2015. Isotropic incompressible hyperelastic models for modelling the mechanical behaviour of biological tissues: A review. Biomedizinische Technik 60 (6), 577–592.

Witz, J.-F., Roux, S., Hild, F., Rieunier, J.-B., 2008. Mechanical properties of crimped mineral wools: Identication from digital image correlation. Journal of Engineering Materials and Technology 130 (2).

Yeoh, O. H., 1993. Some Forms of the Strain Energy Function for Rubber. Rubber Chemistry and Technology 66 (5), 754–771.